The Iranian Journal of Mechanical Engineering Transactions of ISME
Journal homepage: https://jmee.isme.ir/
Vol. 25, No. 1, 2024, pp. 89-111

Research Paper

DOI: https://doi.org/10.30506/jmee.2024.2016680.1335

Designing and Calibrating of a Millinewton Measurement System for Thermal-vacuum Conditions

Morteza Farhid[*]
Assistant Professor

Moharram Shameli[†]
Assistant Professor

Masoud Dehnad[‡]
Ph.D. Researcher

Pendulum-based configuration thrust measurement systems are employed for measuring thrust force of the electrical thrusters in millinewton and smaller orders by separating thrust and weight forces. This paper comprises designing, modeling, manufacturing, calibrating and verifying of a thrust measurement system with inverted pendulum configuration in a range of 5 to 100 mN with resolution of 0.05 mN. Novelty of this system is associated with capability to operate in vacuum condition of 1e-5 mbar and in temperature range within -40°C to +80°C with the desired accuracy. In designing phase, structure of the system and its dimensions are established considering some predefined requirements and criteria using optimization techniques. After detailing modeling and manufacturing phases, an electromagnetic actuator is designed, manufactured and verified for calibration phase. At the last phase, system is verifying through experimental tests and overall uncertainty is calculating. Results show that uncertainty is less than 10% and 2% for the minimum and maximum of the measurement range.

Keywords: Measurement system, Designing, Manufacturing, Calibration, Experimental tests

1 Introduction and literature review

Nowadays utilization of the electrical thrusters is growing for different satellite platforms, ranging from Nano-scale to Large-scale and various missions from orbital transfer to attitude control.

[*]Corresponding Author, Assistant Professor, Space Thrusters Research Institute, Iranian Space Research Center, Tabriz, Iran, m.farhid@isrc.ac.ir
[†]Assistant Professor, Space Thrusters Research Institute, Iranian Space Research Center, Tabriz, Iran, m.shameli@isrc.ac.ir
[‡]Ph.D. Researcher, Space Thrusters Research Institute, Iranian Space Research Center, Tabriz, Iran, m.dehnad@isrc.ac.ir

Received: 2023/11/28, Revised: 2024/02/27, Accepted: 2024/04/14

Electrical thrusters possess general characteristics such as low mass, high specific impulse, low thrust force and exceptionally low thrust-to-weight ratio compared to chemical thrusters. Consequently, any system, which is using for measuring thrust force of the electrical thrusters, should adopts to the abovementioned characteristics. To address this challenge, pendulum-based configuration thrust measurement systems are designed and employed. These systems can separate thrust and weight forces entirely, using counterweights. Therefore, the pendulum-based configuration systems can achieve to very small thrust levels measurement even in Nano-newton orders.

Such systems consist of a rotating arm with the thruster and the counterweights installed at the two ends of it. Thrust force is measured based on the occurred rotation/displacement in the system using a pre-extracted calibration curve. While this procedure is similar for all the pendulum-based configuration systems, they differ in measurement range, accuracy, resolution, rotation/displacement measurement device and employing actuator type.

Thrust measurement system with hanging pendulum configuration is the simplest form of the pendulum-based configuration systems and have been used for decades by many space centers like NASA [1] and ONERA [2]. At equilibrium position of a hanging pendulum system, the arm is configured vertically, with the thruster and counterweights attached to lower and upper ends, respectively. Notable examples of similar systems include thrust stands developed by Nagao et al. [3], Grubisic and Gabriel [4] and Wong et al. [5]. Nagao et al. used knife-edges hinges to minimize friction in millinewton range thrust measurements. A pulley and weight mechanism used for calibration procedure, resulting in measurement error of less than 1.4% in the thrust direction. Grubisic and Gabriel applied a laser-optical-lever principle to afford micro to millinewton range measurement. Wang et al. introduced a non-contact actuator, using magnet, yielding the overall error in calibration coefficient of about 1%.

Furthermore, Nakagawa et al. [6] designed and tested a micronewton range stand with an overall uncertainty of about 8%. More recently, Xu et al. [7] developed a stand for micronewton level thrusters. Their design incorporated an arm which rotated via two thin beryllium copper strips acting as hinges and the calibration was done using an electrostatic actuator. Subsequently, uncertainty reduced to 0.02 micronewton. The system introduced by Wachs and Jorns [8] featured an adjustable counterweight system which enabled the in-vacuum conditions adjustment capability. Additionally, employing a broadband wireless microwave power coupler, which eliminates stiffness and thermal drift introduced by connecting cables, resulted in measurements in micronewton range with a resolution better than 2%

Thrust measurement system with inverted pendulum configuration is similar to the hanging pendulum configuration, except positions of the thruster and counterweights, which are reversed. This configuration leads to augmentation of sensitivity and instability of the system. Cassady et al. [9] presented a simple inverted thrust measurement system in millinewton range with a pulley and weight mechanism for calibration. Following, researchers improved this system through sensitivity raising by mass loading and thermal condition control [10]. Several advantageous design features such as gallium pots for current conduction, optical two-axis displacement sensor, and careful consideration of flexure shape and cooling requirements, reduced the total thrust uncertainty from 20% to 10%.

Inverted pendulum systems support a broad range for thrust measurement and thruster mass. For instance, Xu and Walker [11] designed a null-type inverted pendulum thrust system that supported thrusters having a total mass up to 250 kg and measured thrust within a range of 1 mN to 5 N. In another approach, Neumann et al. [12] designed an inverted pendulum thrust system capable of supporting thrusters with mass up to 50 kg and measuring thrust up to 500 mN. Null-type feature for eliminating thrust alignment error and active cooling system for minimizing thermal effects reduced uncertainty of thrust measurements to about ±0.6%. Kokal and Celik [13] and Harmann and Dartsch [14] introduced inverted pendulum systems using thin

steel strips as hinges, enabling thrust measurement in range of sub-millinewton to hundreds of millinewton. Moreover, Kokal and Celik [15] improved their previous system and made it capable of changing the thrust measurement range and its resolution and also in-situ null position adjustment.

Among recent researches, it is worth mentioning the system developed by Asakawa et al. [16] with thrust measurement range within 1 to 10 mN. The calibration procedure allowed achieving a resolution of 80 μN for thrust measurement and 0.01 g for mass loss measurement, by taking into account any zero position drift caused by propellant consumption. In addition, Scharmann et al. [17] compared results of an inverted pendulum thrust in range of sub-millinewton with direct measurement, using a force probe and a Faraday-array scanner.

Main difference of torsional pendulum thrust measurement systems, lies in axis of the rotation which is aligned parallel to the Earth gravity direction. In other words, plane of the rotation in this type of systems is parallel to the horizon, thus the gravitational force has no effect on the rotation. This configuration arises more sensitivity and stability to the system, therefore, made the torsional pendulum systems to be suited for thrust measurement in micronewton and nanonewton levels.

Torsional pendulum thrust measurement systems introduced by Yang et al. [18], Kolbeck et al. [19], Marques et al. [20, 21] and Zhang et al. [22] were operating within micronewton range. The system developed by Yang et al. with specially suspending design and precise assembly, could measure thrust up to 264 μN with nanonewton resolution and load capacity up to several kilograms. Kolbeck et al. designed, calibrated and tested a torsional system with measurement range from 2.5 μN up to 30 μN. Moreover, the system presented by Marques et al. and Zhang et al. were capable of measuring thrust within the ranges of 25 up to 330 μN and 2 up to 30 μN, respectively. Measurement range for torsional pendulum configuration systems is extended to millinewton range as well, such as systems presented by Zhang et al. [23] which featured maximum measurable thrust of 2.7 N and resolution of 0.1 mN.

Furthermore, in order to increase sensitivity of thrust measurement for any type of systems, certain methods have been employed such as signal analysis techniques for noise characterization [24], drag-free techniques include constantly adjustable thrust and fast response time [25] and utilization of Galinstan for frictionless liquid-metal instrumentation and power feeds [26].

This paper presents a comprehensive process of designing, modeling, manufacturing, calibrating and verifying of a thrust measurement system with inverted pendulum configuration. The reasons for the selected configuration are lie to the predefined requirements including the thrust measurement range, the thruster mass support capacity, and the geometrical dimensions. The thrust measurement system is expected to operate in vacuum condition of 1e-5 mbar and in temperature range within -40°C to +80°C. Indeed, the requirement for operating in a thermal-vacuum condition, underlines the novelty of the developing system. After the designing phase, the system is modeled and manufactured. For calibration, an electromagnetic actuator is designed, manufactured and verified. Finally, the system is verified through experimental tests and overall uncertainty is obtained.

2 Designing phase

The intended thrust measurement system is designing by considering a set of predefined requirements, which are:

1) Thrust measuring range of 5 to 100 mN with resolution of 0.05 mN,
2) Thruster mass support capacity of 5 Kg,
3) Capable to operate in vacuum condition of 1e-5 mbar,
4) Capable to operate in temperature range of -40°C to +80°C,

5) Satisfying maximum geometrical dimension of 500x500x500 mm, and
6) Not to exceed maximum mass of 20 Kg.

Based on these requirements and review of the literature, inverted pendulum configuration can fulfil the requirements completely. Additionally, abovementioned requirements exert a couple of design criteria, include:

1) Displacement of the system should be within a range which can be determined by a displacement measurement sensor capable to operate in the predefined thermal-vacuum condition.
2) Structure of the system should have enough strength to support 5 kg thruster load with minimum sensitivity to temperature variations.
3) A damping mechanism should be utilized for vibrations and fluctuations suppression in order to reduce settling time and enhance accuracy.
4) An appropriate actuator should be selected or designed for calibration procedure which is capable to operate in the predefined thermal-vacuum condition effectively.
5) Thruster should be in a fixed orientation during motion to prevent any error due to thrust vector misalignment.
6) Motion of the system should be frictionless and predictable.

Designing phase is composed of three subsections include structure design, hinge design and thermal design considering the aforementioned requirements and criteria.

2.1 Structure design

The first step in the designing phase is deriving an analytical model for motion of the system. A schematic drawing of the system is depicted in Figure (1), illustrating both the two equilibrium and rotated positions. Structure of the system consists of two horizontal mount-plates and two vertical arm-plates, all connected by hinges. The configuration uses two-parallel-arm mechanism ensuring that two mount-plates remain in the horizontal orientation. Also, two vertical arm-plates are joined to an external fixed frame by hinges.

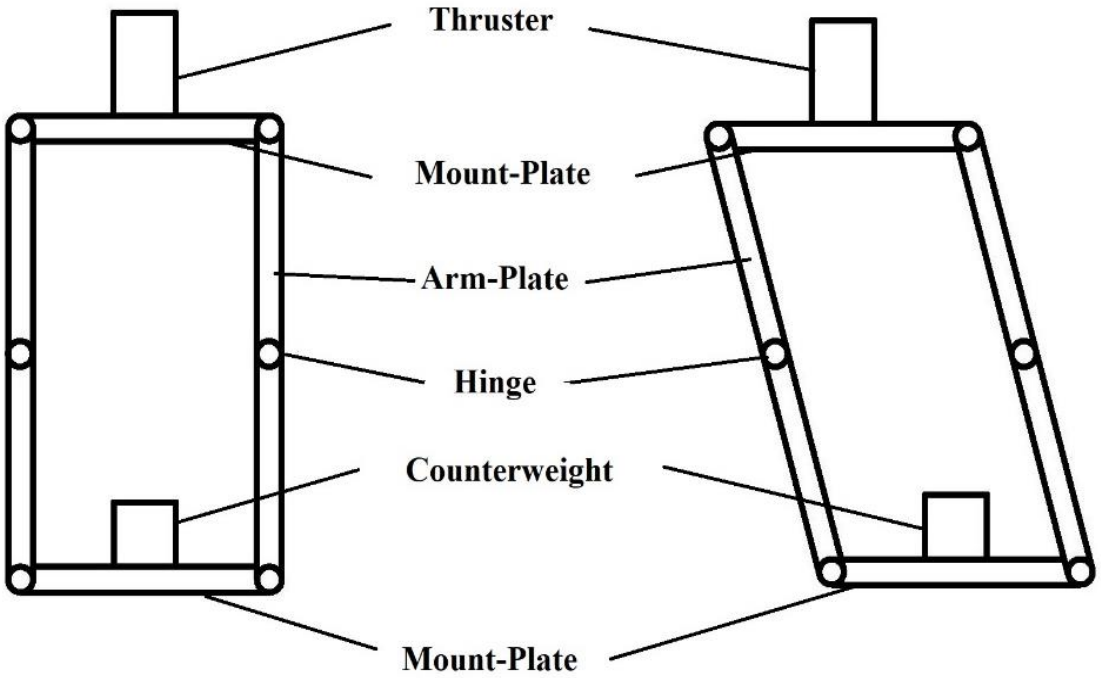

Figure 1 A schematic drawing of the system in neutral and rotated positions.

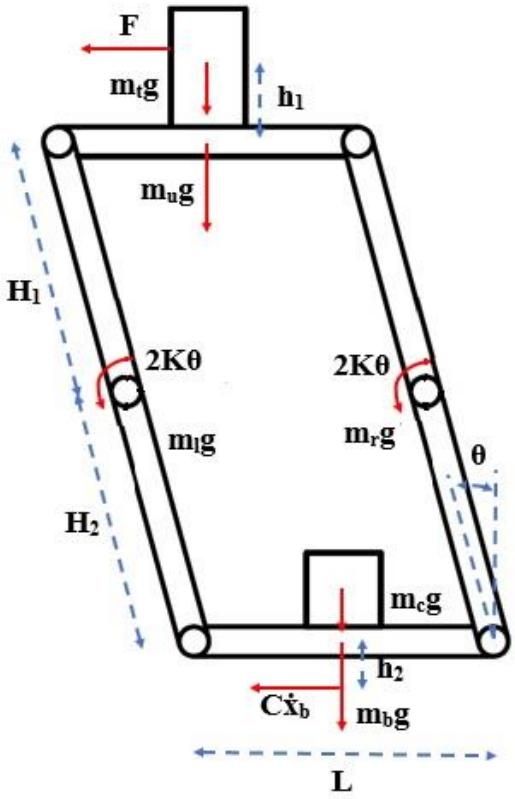

Figure 2 Free-body-diagram of the system

A damping mechanism, based on the eddy current phenomena is employed to suppress the induced vibrations and fluctuations. This mechanism consists of a conductive (copper) plate moving in a magnetic field created by permanent NdFeB magnets. This is a common damping mechanism with a proven record of success in similar thrust measurement systems [8, 15, 22]. The damping can be tuned by adjusting strength, size, number, and polarization of the permanent magnets besides thickness of the copper plate and distance between the magnets and the plate.

To develop the analytical model for motion of the system, free-body-diagrams of the system and all parts are drawn such as one shown in Figure (2) along with the relevant parameters. By means of the force equilibrium relations, equation of motion of the system can be derived as Eq. (1) which is detailed in reference [15]:

$$\begin{aligned}\ddot{\theta}\left[J - J_u - J_b + (m_c + m_b)\left(H_2^2 + H_2 {}^{L}/_{2}\,\theta\right) - (m_t + m_u)\left(H_1 H_2 + H_1 {}^{L}/_{2}\,\theta\right)\right] \\ + \dot{\theta}^2\left[(m_c + m_b)H_2 {}^{L}/_{2} - (m_t + m_u)H_1 {}^{L}/_{2}\right] + \dot{\theta} C H_2^2 \\ - \theta\left[(m_t + m_u)gH_1 - (m_c + m_b)gH_2 - 12K\right] - FH_1 = 0\end{aligned} \tag{1}$$

In static equilibrium, rotation of the system is equal to:

$$\theta = \frac{FH_1}{(m_t + m_u)gH_1 - (m_c + m_b)gH_2 - 12K} \tag{2}$$

Moreover, fundamental frequency of the system can be computed using Eq. (3). The fundamental frequency becomes important when the system undergoes dynamic loads such as vibrations caused by vacuum pumps. In this case, it is preferred to take away the fundamental frequency from working frequency of the pumps.

$$\omega = \sqrt{\frac{12K + (m_c + m_b)gH_2 - (m_t + m_u)gH_1}{J - J_u - J_b + (m_c + m_b)\left(H_2^2 + H_2 {}^{L}/_{2}\,\theta\right) - (m_t + m_u)\left(H_1H_2 + H_1 {}^{L}/_{2}\,\theta\right)}} \quad (3)$$

From the above equations, static rotation of the system and its fundamental frequency are influenced by mass of the thruster, the counterweights and mass of the mount-plates as well as length of the arm-plates, location of hinge in the arm-plates and stiffness of the hinges. Increasing stiffness of the hinges causes reduction in static rotation of the system while elevating the fundamental frequency. It should be mentioned that each mount-plates is connected to the arm-plates via four hinges and each arm-plate is joined to the external frame through two hinges, making total of 12 hinges in the system.

Figure (3) shows effects of length of the arm-plates and location of hinge in the arm-plates on performance of the system. As depicted in Figure (3-a), when rotation-arm of the upper mount-plate (H_1) remains constant, as rotation-arm of the lower mount-plate (H_2) increases, rotation of the system decreases significantly. Figure (3-b) presents effect of increasing rotation-arm of the upper mount-plate (H_1) keeping constant rotation-arm of the lower mount-plate (H_2), which yields to rise in rotation of the system. Consequently, longer arm-plates are favored as they lead to higher sensitivity and accuracy by increasing rotation of the system. Nevertheless, it is important to note that longer arm-plates increase volume and mass of the system also.

In order to find an optimized design for the structure, Genetic Algorithm is used. To this end, a cost function is defined in form of difference between predefined geometrical requirements and achieved geometrical requirements as presented in Eq. (4). The considered requirements are total mass of the structure, length of the arm-plate and rotation of the system. Within the optimization process, each chromosome consists of six genes representing the geometrical parameters, namely, rotation-arm of the upper mount-plate, rotation-arm of the lower mount-plate, stiffness of the hinge, mass of the upper mount-plate, mass of the lower mount-plate and counterweights.

$$Z = \sum_{n=1}^{3} \left| \frac{C_{specified}{}_n}{C_{achieved}{}_n} - 1 \right| \quad (4)$$

The predefined geometrical requirements are established as 20 Kg for total mass of the structure, 300 mm for length of the arm-plate and 1 mm for rotation of the system at thrust of 100 mN. These requirements are defined due to some physical constraints such as handling and transportation limitations and volume increasing issues considering the utilized vacuum-chamber size.

Additionally, the permissible ranges for variations of the abovementioned geometrical parameters are specified within the predefined geometrical requirements. By solving the optimization process for a population of 50 individuals, convergence is achieved after 200 iterations, with a cost function value of 6e-4. The obtained optimal geometric dimensions are listed as followings:

$$\begin{cases} H_1 = 120\ mm \\ H_2 = 180\ mm \\ m_u = 2.5\ Kg \\ m_b = 1.2\ Kg \\ m_c = 6\ Kg \\ K = 0.015\ Nm/rad \end{cases} \quad (5)$$

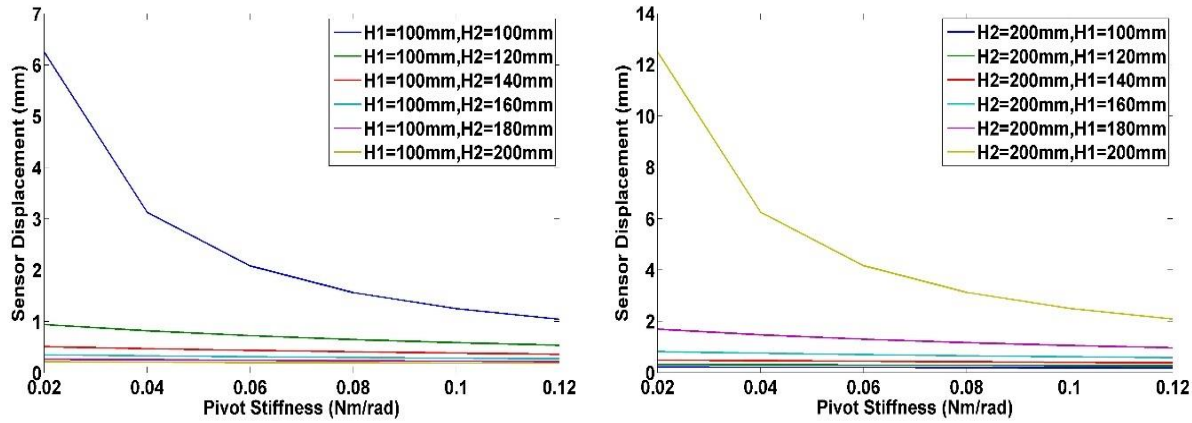

(a) **(b)**

Figure 3 Effects of length of the arm-plates (**a**) and location of hinge in the arm-plates (**b**) on performance of the system

2.2 Hinge design

The second step in the designing phase is appertained to hinges of the structure. These hinges should rotate without any friction, flexible easily and withstand against applied load without any plastic deformation or degradation in their specifications through their operational life and within the expected temperature range. Commercially available flexure hinges have been used in the similar systems effectively. However, in this research, an alternative type of frictionless hinge will be developed, known as strip hinges. It must be pointed out that deformations in all 12 hinges within the structure are uniform due to the geometrical configuration of the system. As depicted in Figure (4), a strip hinge can be simplified as a two-dimensional single-ended one degree-of-freedom beam subjected to a concentrated uniform distributed force at its end. Within this assumption, behavior of the beam can be governed by the Euler-Bernoulli beam theory and its deflection and maximum magnitude are formulated with the Equation (6).

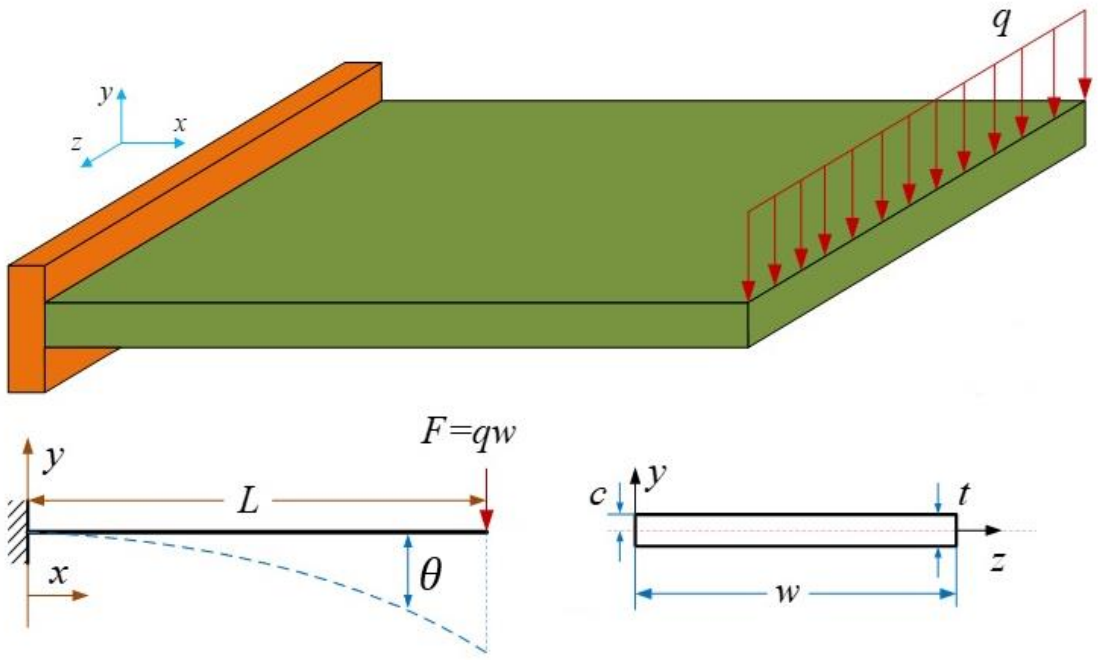

Figure 4 Simplified free body diagram of strip hinge as a cantilever beam

$$\theta(x) = \frac{Fx}{2EI}(x - 2L) \xrightarrow{x=L\rightarrow\theta=\theta_{max}} |\theta_{max}| = \frac{FL^2}{2EI} \tag{6}$$

By rearranging the above equation, torsional stiffness of the strip hinge can be represented by ratio of bending moment to deflection as follow:

$$K_t = \frac{M}{\theta} = \frac{Ewt^3}{6L} \tag{7}$$

To investigate effects of geometric parameters of the hinge (length, width, and thickness) on its dynamic characteristics, torsional stiffness of the hinge is assessed utilizing the above equation. Figure (5) shows variations in torsional stiffness of the hinge in relation to changes in the geometric parameters. The results collectively reveal that length of the hinge has the most substantial impact on its torsional stiffness.

To devise an optimized design for the hinge, an optimization process for geometric dimensions of the hinge (optimization parameters) is applied. A cost function is defined which comprises summation of the hinge's mass along with ratio of the von-Mises stress to the yield strength of material, both of which are essential to the optimal design. It should be noticed that these two terms are in a same order. Mass of the hinge is in order of 1e-1 in grams, same as the ratio of the von-Mises stress to the yield strength. Boundary condition of the optimization problem entails an achievable predetermined rotation.

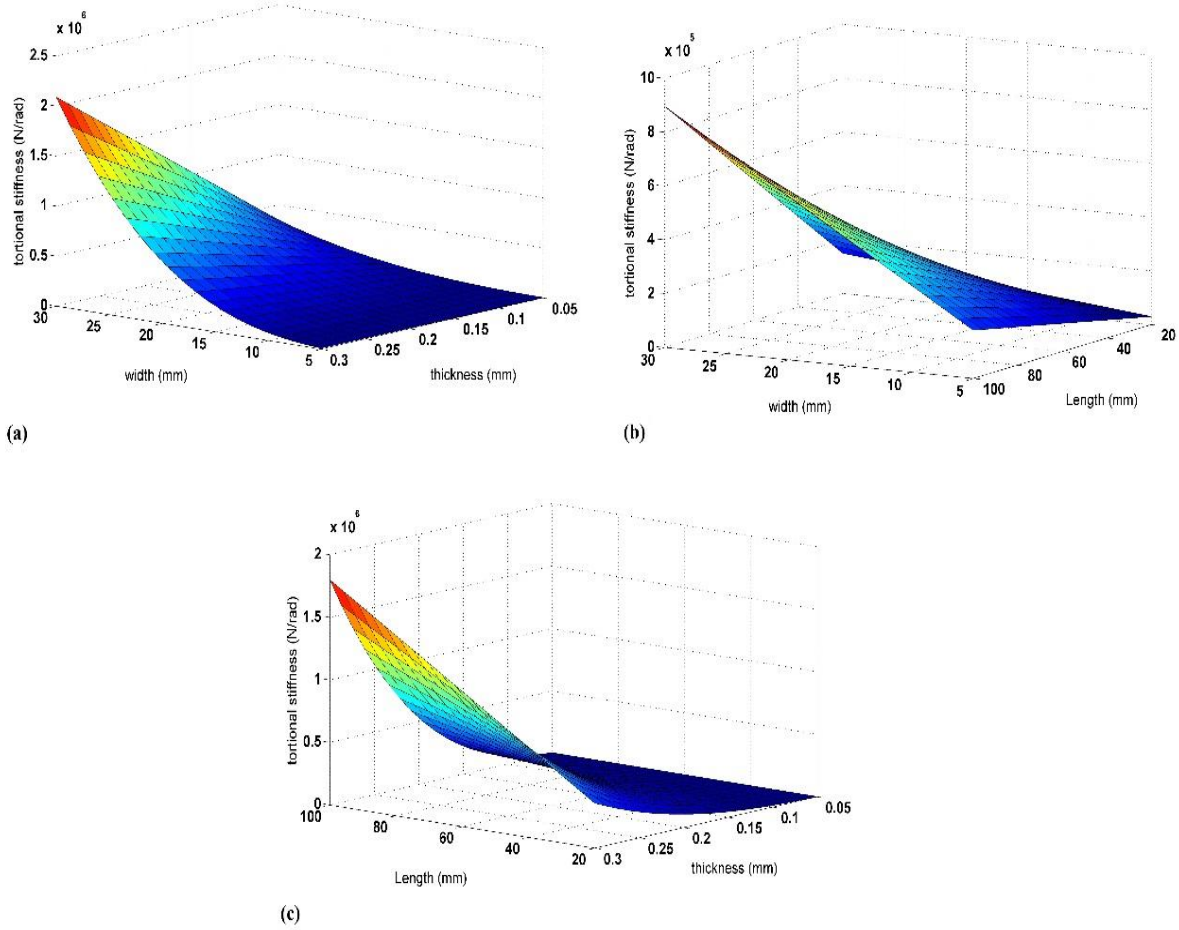

Figure 5 Effects of geometric dimensions on the torsional stiffness: (**a**) cross section, (**b**) length and width, (**c**) length and **t**hickness

As such, the ensuing nonlinear optimization problem takes the form presented below:

$$\begin{cases} \min\limits_{L,w,t} \dfrac{\sqrt{\sigma_b^2 + \sigma_a^2}}{\sigma_y} + (Lwt)\upsilon g \\ s.t \quad \theta_{max} \le \theta_{cte} \end{cases} \tag{8-a}$$

$$\sigma_a = \frac{F_n}{wt} \tag{8-b}$$

$$|\theta_{max}| = \frac{6FL^2}{Ewt^3} \tag{8-c}$$

Within the cost function formulated in Eq. (8-a), it becomes evident that the function is characterized by a linear term associated with weight, and a nonlinear term comprising fractional and radical expressions tied to stress criteria. Furthermore, by integrating Eqs. (8-b) and (8-c) into the cost function, the optimization parameters are incorporated into a fractional radical expression. Thus, the optimization problem emerges as a nonlinear, multivariable problem constrained by a nonlinear boundary condition.

In order to solve the defined optimization problem, an interior point algorithm is utilized. To this end, the transverse force magnitude is set at 5 N, the axial force magnitude at 5 N, and t maximum rotation angle of the hinge at 5 deg. Moreover, the permissible ranges for variation of three geometric dimensions of the hinge, i.e., length, width, and thickness, are specified as [10, 100], [10, 50], and [0.05, 0.5] mm, respectively. The selected material is steel 300 series, characterized by an elasticity modulus of 205 GPa and a yield strength of 200 MPa. Convergence is achieved after 27 iterations, meeting the established tolerance of approximately 1e-16, thereby identifying a minimum point within the specified interval. The optimal geometric dimensions are obtained as followings:

$$\begin{cases} L_{op} = 27.221\ mm \\ w_{op} = 20\ mm \\ t_{op} = 0.097\ mm \end{cases} \tag{9}$$

Ultimately, the final geometric dimensions are selected as Eq. (10), based on manufacturing limitations:

$$\begin{cases} L = 30\ mm \\ w = 20\ mm \\ t = 0.1\ mm \end{cases} \tag{10}$$

2.3 Thermal design

As mentioned at the beginning of this section, the system's operation is mandated within a vacuum condition of 1e-5 mbar and temperature range from -40°C to +80°C. Main outcome of posing to such temperature variations is dimensional deformation in structure of the system. On the other hand, accurate operation of the system precept to reduce any possible dimensional change in the structure. In the predefined thermal-vacuum condition, heat transfers for the structure occurs through conduction and radiation.

To reduce thermal effects, three approaches are considered. The first approach is anodizing the whole structure in order to decrease thermal conductivity.
Next, structure of the system is insulated from the thruster and chamber's interior surfaces using insulating material, minimizing conduction as possible. The final consideration is covering the whole system by polished copper plates, to reflect and absorb the thermal radiation and shielding the interior components from radiation exposure. It is expected that the above considerations collectively contribute in reduction of dimensional changes in the structure, guaranteeing required measurement accuracy. Moreover, complete thermal simulation will be conducted in the following section.
Another important issue in thermal designing, is the selection of appropriate instruments. Two instruments are utilized in the system, a LVDT sensor for displacement measurement and a loadcell for capturing applied force by the actuator. Both of these sensors must be capable of operating in the specified temperature range. Additionally, LVDT and loadcell sensors should have a minimum resolution of 1 μm and 0.01 mN, respectively, while their measurement range should align with the system's requirements.

3 Modeling

Taking into account the predefined general requirements and the consequent design criteria and based on the outcomes from the previous section, final design of the thrust measurement system is modeled as seen in Figure (6) without the copper covering plates and in Figure (7) with addition of these plates.
All parts are precision machined from aluminum 7000 series, a common material for space thermal-vacuum conditions. The strip hinges fabricated through laser-cutting from steel 300 series which is a ferromagnet material and does not affected by environmental electromagnetic field. The final dimensions of the system are 420, 400 and 350 millimeter in height, width and depth, respectively, with a total mass of the system less than 15 kg. Moreover, the strip hinges have bending stiffness of 0.011 Nm/rad. Accordingly, the linear displacement of the system is 742 μm for 100 millinewton thrust, calculated by Eq. (2). Given linearity of the system, the displacement for 5 millinewton thrust force is about 37 μm.
The damping mechanism is located beneath the lower mount-plate for space-saving purposes. This mechanism consists of a 5 mm thickness copper plate which is placed between six cubic NdFeB permanent magnets of dimension 40x20x5 mm with grade N42 magnetization.

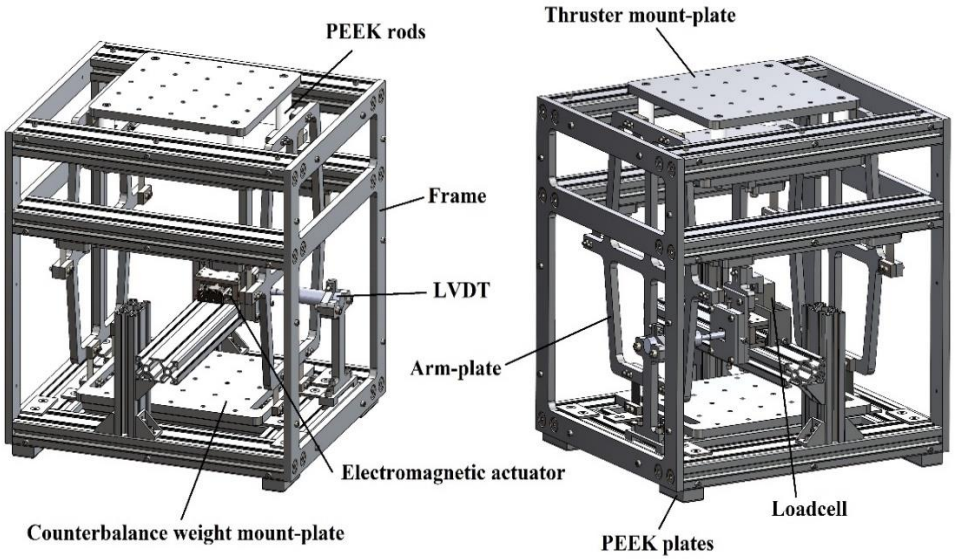

Figure 6 Final design of the thrust measurement system

Figure 7 Copper covering plates of the thrust measurement system

Furthermore, all surfaces of the system are covered by 1 mm thick copper plates. The upper mount-plate is connected by four PEEK rods to the main structure, chosen for its excellent insulating properties and mechanical strength specifications. Additionally, four PEEK rods are mounted under the frame, to insulate the system from the thermal-vacuum chamber's interior surfaces.

4 Thermal simulation

To validate the thermal design of the thrust measurement system, a thermal finite element analysis is carried out. Thermal load in form of radiation is applied to all surfaces of the structure. Duration of exposure is set to two hours according to the relevant standards like ECSS. Simulation results in the form of temperature distribution, for both cold (-40°C) and hot (+80°C) exposures, are illustrated in Figure (8). It is assumed that the initial temperature is equal to 22°C. For better visualization, the covering copper plates are removed, allowing to a clear view of the temperature distribution within the interior components of the structure.

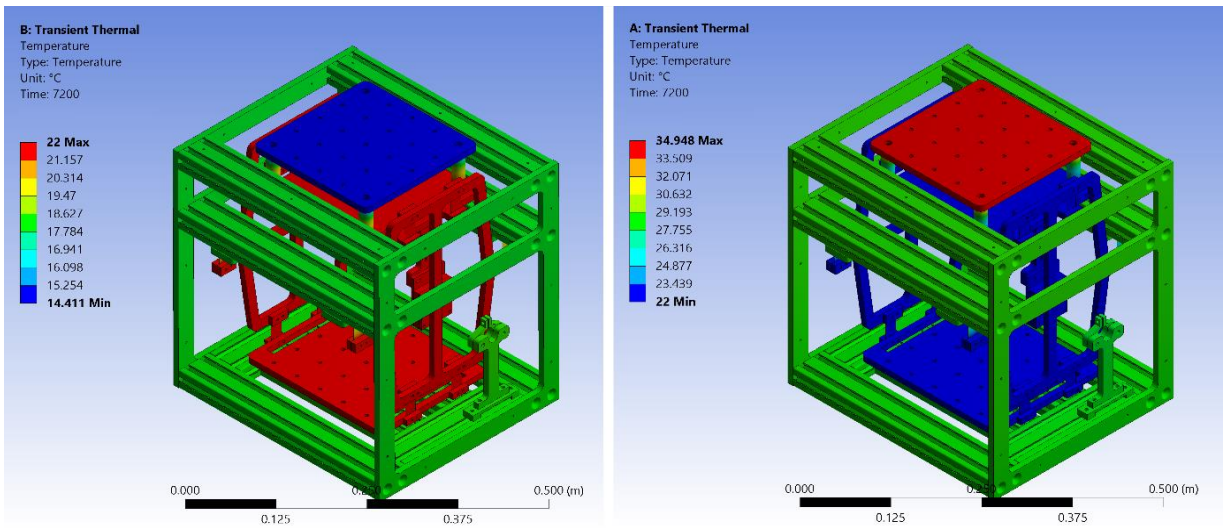

Figure 8 Temperature distribution in the structure for cold and hot exposures

Observing Figure (8), in cold/hot condition, the upper mount-plate which is exposed to the radiation directly, has the minimum/maximum temperature. Whereas, temperature of the frame is decreased/increased to about 17°C/29°C, remarkably, temperature of the interior components remains only slightly below/above the initial condition. It could be concluded that the employed approaches for thermal control are efficient and proficient. Hence, it is expected that the temperature variations will not affect the measurement considerably.

5 Calibration and verification

One of the main steps in designing a thrust measurement system is calibration. Calibration procedure is a prominent and significant task in verification and validation of operation of the system. Generally, the operation of a thrust measurement system can be assessed and qualified via six criteria: sensitivity, repeatability, accuracy, resolution, predictability and response time [27]. In fact, the calibration procedure not only prescribes these criteria but also establishes the relation between the thrust and displacement of the system under environmental conditions which is similar to the thruster's testing environment. Additionally, the employed actuator in the calibration procedure plays an important role. The actuator must be compatible with the testing environment including thrust range and thermal-vacuum conditions.
Subsequent to manufacturing the thrust measurement system, calibration becomes necessary. The calibration procedure is conducted in the room temperature alongside in the cold (-40°C) and hot (+80°C) conditions, all in vacuum pressure using an appropriate actuator. The following subsection describes the process for attaining an appropriate actuator. Outcome of the calibration procedure is calibration equation (curve) which represents the relation between the thrust and displacement of the system. In case of testing a thruster, the occurred displacement in the system is measured using LVDT sensor and the equivalent thrust force is estimated by means of the extracted calibration equation.

5.1 Actuator design

Various types of actuators have been employed in calibration procedure of the inverted pendulum thrust measurement systems such as mass and pulley mechanism, hammer, piezoelectric actuator, electrostatic actuator and electromagnetic actuator. The latter two types are more accurate, acceptable and favored because of their non-contact operation, precise and continuous motion without mechanical hysteresis, fluctuations and backlash, lower power-to-volume ratios compared to contact-based actuators, and capability to be designed in various sizes, shapes, motion ranges, configurations, and capacities [28, 29].
A linear voice coil is an electromagnetic actuator that operates by passing electric current through embedded coils within a magnetic field, which is created by permanent magnets. This mechanism generates the Lorentz force and is facilitated by the phenomenon of self-induction. Here, a low power linear voice coil will be designed, manufactured and validated which is intended to generate millinewton forces suitable for calibration of the presented system. The main focus for designing are achieving geometric compactness, weight efficiency, and maintaining a consistent force throughout its motion range. Schematic representation for geometric configuration of the proposed voice coil is depicted in Figure (9). The actuator encompasses two sets of permanent magnets, positioned both above and below a central coil and are magnetized perpendicular to it (shown as yellow lines). The actuator force is calculated by evaluating the Lorentz force exerted on the coil due to the magnetic field (shown as green lines). The magnetic flux density within the spatial region between the permanent magnets, wherein the coil is positioned, is deduced analytically employing Maxwell's law and the surface charge methodology, as detailed by Rovers et al. [30] and Furlani [31].

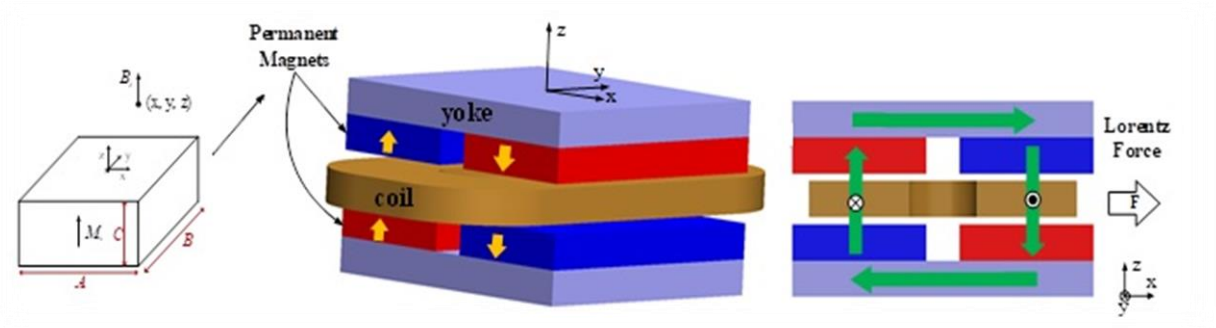

Figure 9 Arrangement illustration of linear voice coil and its analytical magnetic field visualization

Assuming homogeneous magnetization and cuboidal geometric shape for the magnets (as seen in Figure (9)), alongside the fact that the voice coil is designed to take advantage of the strongest component of the magnetic field, the z-component of the magnetic field at a specified position is computed as following in accordance with reference [32, 33]:

$$B_z = \frac{\mu_0 M_s}{4\pi} \sum_{i=0}^{1} \sum_{j=0}^{1} \sum_{k=0}^{1} (-1)^{i+j+k} \tan^{-1}\left(\frac{ST}{RU}\right) \tag{11}$$

where the final term in Eq. (10) aligns with the geometric considerations outlined in Figure (9), as written below:

$$\begin{aligned} S &= x - (-1)^i \left({}^{A}/_{2}\right), \\ T &= y - (-1)^j \left({}^{B}/_{2}\right), \\ U &= \left(z + {}^{C}/_{2}\right) - (-1)^k \left(- {}^{C}/_{2}\right), \\ R &= \sqrt{S^2 + T^2 + U^2}. \end{aligned} \tag{12}$$

Comprising four magnets, the voice coil's collective magnetic field effects on the coil emerges from superposition of the individual magnetic fluxes as Eq. (11). It should be noted that undesired force which is arises from generation of a perturbing force in the curved portion of the coil is mitigated. To compute electromagnetic force acting upon the coil, relationships outlined by the Lorentz's law are incorporated as detailed by Compter et al. [34].
Considering a symmetry configuration for the voice coil and ignoring the negligible x-component of the magnetic field, formulation for the Lorentz force exerted by the voice coil is presented as follow, where the geometrical parameters are depicted in Figure (10).

$$F = 2\left(\frac{w_c}{d_c} - \frac{1}{2}\right)\left(\frac{2}{\sqrt{3}}\left(\frac{h_c}{d_c} - 1\right) + 1\right)\frac{l_c i}{A}\int_A \left(B_{z,right}\right) dA \tag{13}$$

For designing a voice coil, some geometric parameters should be specified. These parameters are categorized into two distinct groups: predetermined and independent. Parameters such as diameter of wire, thickness of coil, width of magnet, and coil current fall into the independent category, while other factors are set as predetermined constants. Usually, a specification is defined for the voice coil representing efficiency designated as voice coil constant (as ratio of the force to the current).

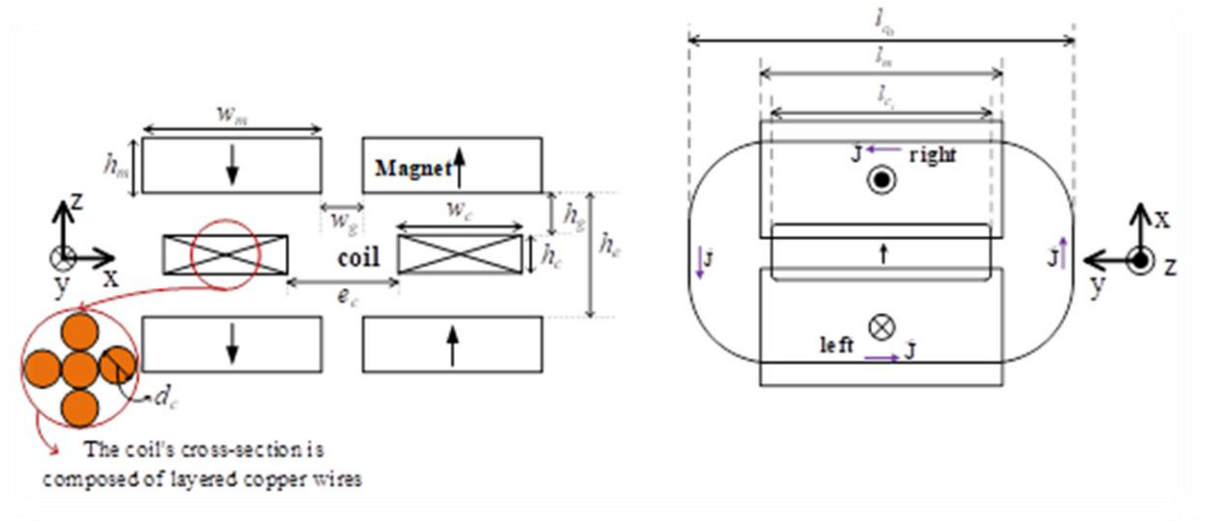

Figure 10 Geometric parameters of linear voice coil

Figures (11) presents graphical depictions that highlight variations in the force constant and the ohmic loss versus variation in independent parameters.

Observing Figure (11-a), it is evident that augmenting the coil width is accompanied by concurrent increases in both the force constant and the ohmic loss. Furthermore, as width of the magnet increases, the force constant also rises as shown in Figure (11-b), while the ohmic loss remains consistent. Figure (11-c) underscores that increasing diameter of wire yields a reduction in both force constant and heat loss. While this reduction in ohmic loss is advantageous, an excessive wire diameter reduces the force constant. Consequently, aligning with the objective of achieving a force constant near 1, the optimal selection for diameter of wire is 1 mm. In this state, a force constant of 0.97 (N/A) is achievable.

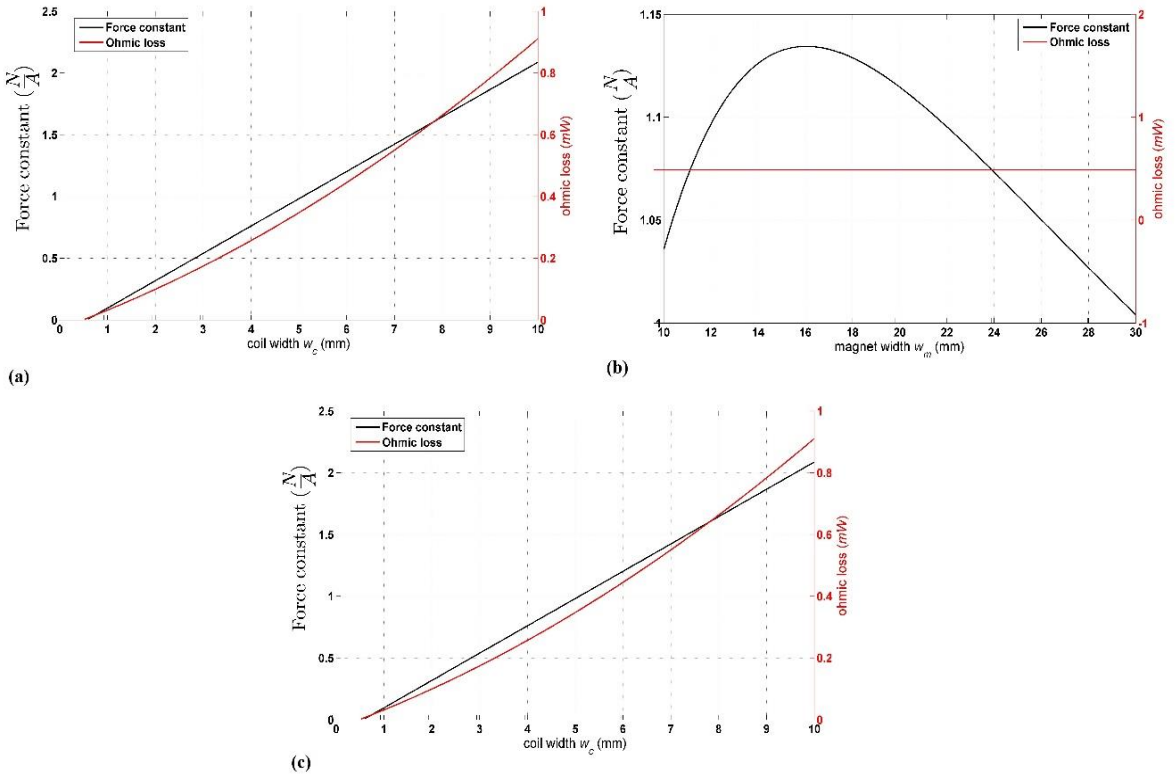

Figure 11 Variations in the force constant and the ohmic loss versus variation in a) width of the coil, b) width of the magnet, and c) wire diameter

Furthermore, Figure (12-a) outlines variations in induced force within the voice coil and corresponding ohmic loss. Notably, the figure reflects a linear correlation between current and force (force constant). Additionally, Figure (12-b) illustrates nearly uniform actuator force throughout its course of motion. Finally, Figure (13) depicts CAD model of the designed voice coil. The thickness of coil aligns with the diameter of wire, while the coil features 5 turns within the x-y plane.

Subsequent to manufacturing, a series of experimental tests are devised to validate the voice coil. As illustrated in Figure (14-a), the experimental setup adheres to a methodology commonly employed in the literature such as references [15, 32]. The voice coil is positioned upon a precision scale oriented along the motion axis. The utilized scale has nominal accuracy of 0.01 gr. Various current values are applied to the coil correspondingly generate associated readings on the scale, representative of the induced force. The experimental results alongside the counterparts computed from analytical relations are depicted in Figure (14-b). The mean squared errors of the measured force data are 0.01, which validate the designed and manufactured actuator.

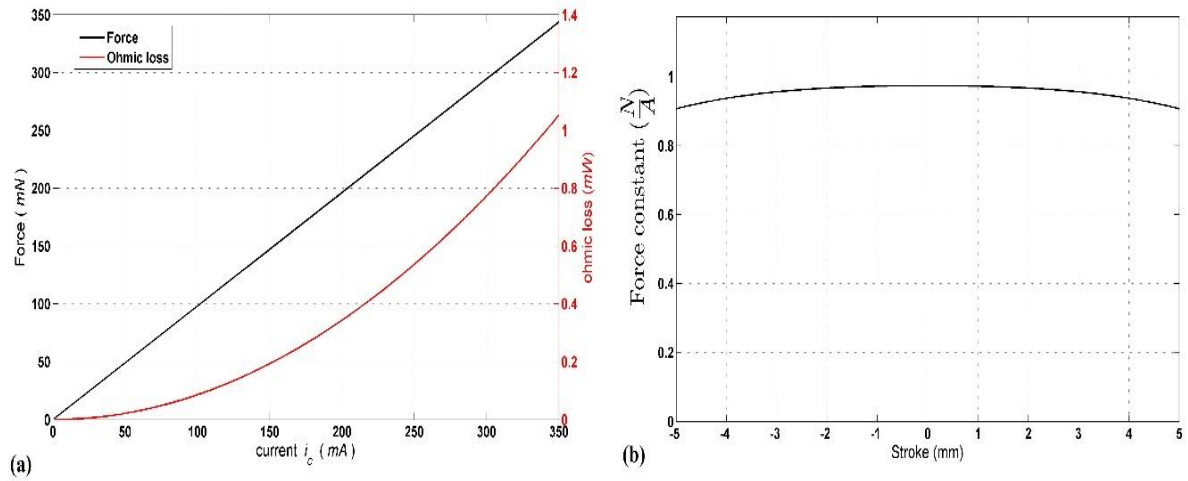

Figure 12 a) Variations in the force and the ohmic loss versus variation in current intensity, and **b**) force constant behavior along voice coil motion range.

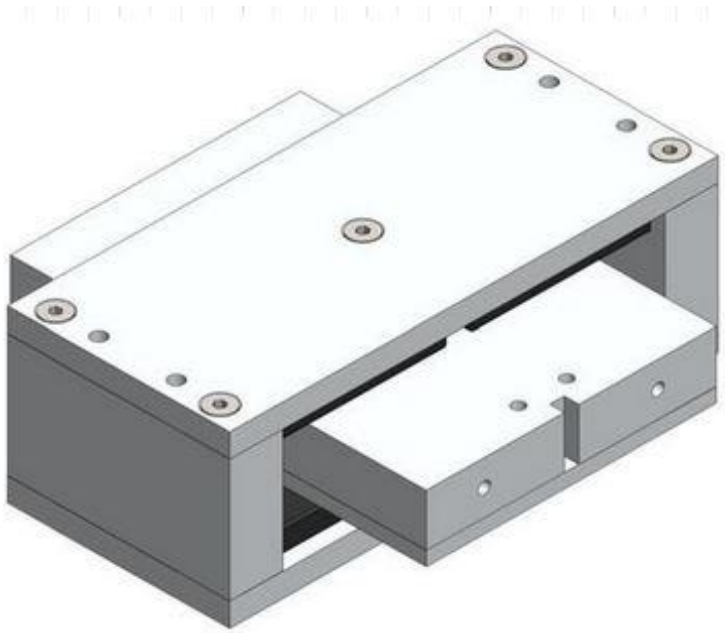

Figure 13 CAD model of designed voice coil

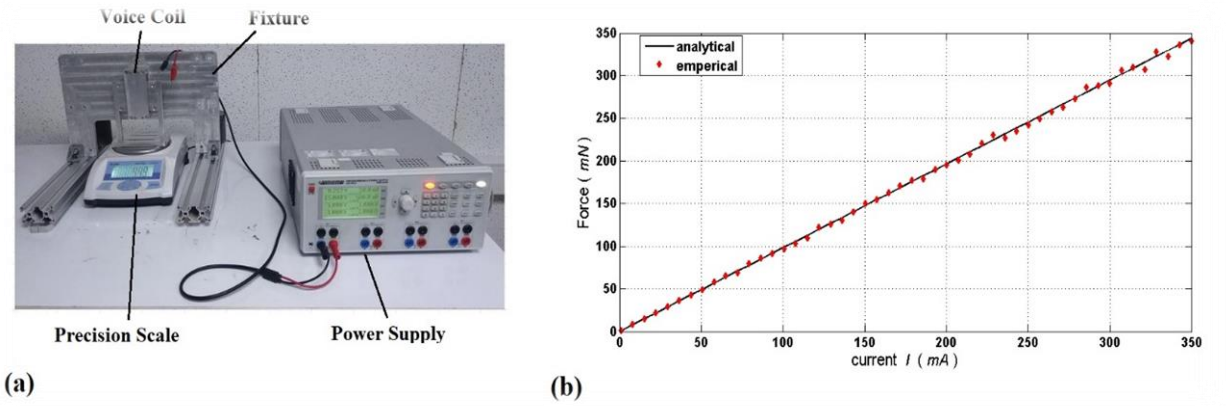

Figure 14 a) Setup for validation experiments, and **b**) experimental and analytical results for induced force.

5.2 Calibration procedure

The calibration procedure of the thrust measurement system is conducted in a thermal-vacuum chamber as demonstrated in Figure (15). A set of dummy weights equal to 5 Kg is placed on the upper mount-plate, while, equivalent counterweights are placed on the lower mount-plate. Once the vacuum reaches the pre-defined value of 1e-5 mbar, the system is calibrated at the room temperature. Next, the chamber is chilled and the temperature is decreased to -40°C. After two hours, the system undergoes calibration again. The final part of the calibration procedure is done at temperature of +80°C. To this end, the chamber is heated and the calibration completes after two hours in the mentioned temperature.

Using the thermal design considerations, temperature of the copper plates and LVDT mounting rod after two hours in the cold and hot conditions, reached just to -12°C and -2°C for the cold exposure and 44°C and 29°C for hot exposure, respectively. The aforementioned temperatures captured by two K-type thermocouples, are which embedded using thermo-resistive adhesive tape. These results verify the thermal design of the system and validate its capability to operate within thermal-vacuum conditions.

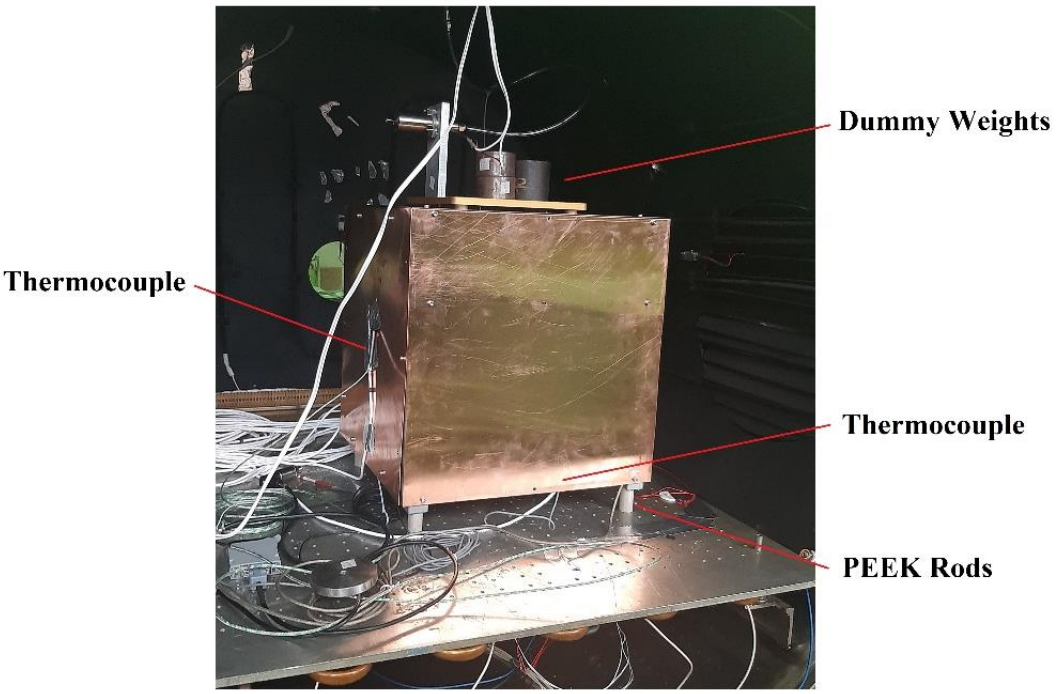

Figure 15 Thrust measurement system in the thermal-vacuum chamber

The calibration procedure should cover the expected thrust range and involves a minimum of three points (sufficient to fit a linear curve). To enhance accuracy, it has been recommended to repeat the calibration at each point [27]. For the studying system, the calibration procedure is conducted at 5 points (5, 25, 50, 75 and 100 mN) and repeated three times. Root mean square of the results are listed in Table (1). Moreover, a calibration curve is extracted for each set of calibration data and plotted in Figure (16).

It is evident from the calibration data that, the required current to generate a certain induced force is influenced by temperature variations. As the environment temperature diverges more from the room temperature, the required current is reduced, where this reduction is more obvious in the cold condition. Furthermore, for a certain induced force, the occurred displacement is increased by the temperature rising. Another important observation, is linearity of the system which could be seen for all three calibration curves. Thus, it could be concluded that thermal conditions significantly impact the thrust measurement system, the actuator and the calibration procedure, which must be considered during thrusters testing.

Table 1 Calibration results in different thermal condition

Temperature = 25°C			Temperature = -40°C			Temperature = +80°C		
Actuator current (mA)	Induced force (mN)	Displacement (mm)	Actuator current (mA)	Induced force (mN)	Displacement (mm)	Actuator current (mA)	Induced force (mN)	Displacement (mm)
5	4.84	0.063	3	4.75	0.029	4	5.12	0.088
26	25.20	0.356	18	25.05	0.142	22	25.13	0.432
52	50.41	0.719	41	49.71	0.278	47	50.23	0.839
78	75.59	1.069	68	75.28	0.418	74	74.76	1.245
103	99.81	1.443	96	100.06	0.565	100	100.39	1.687

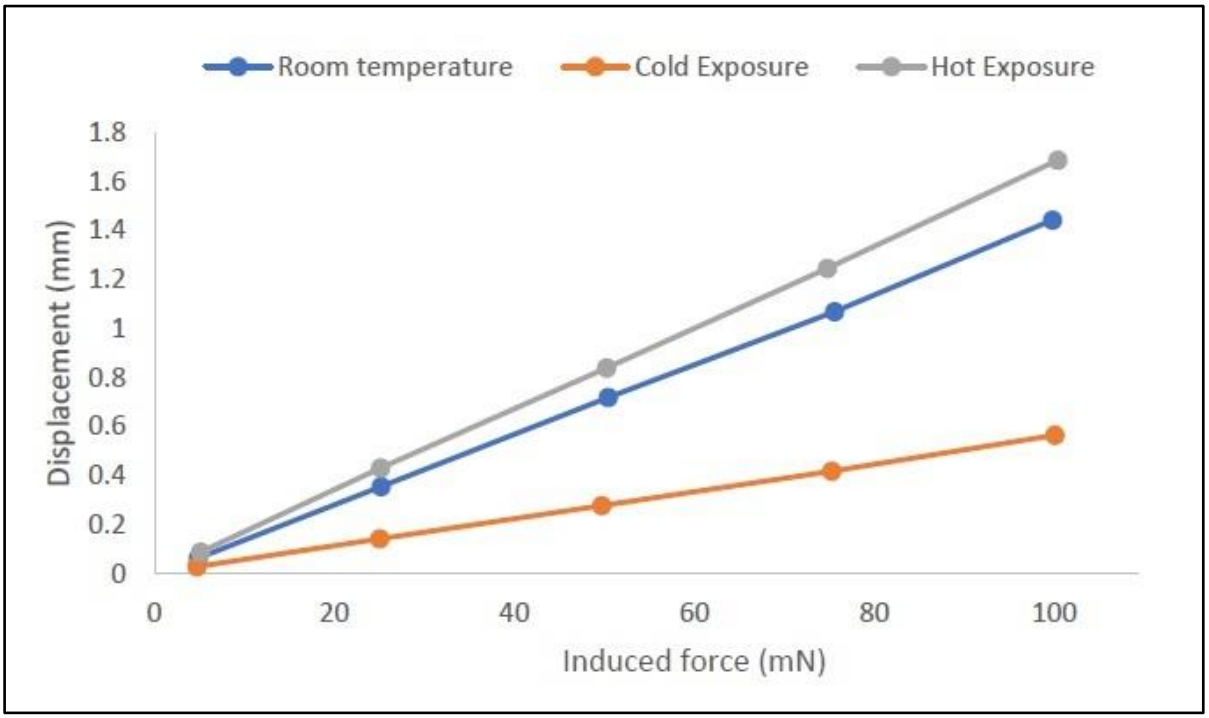

Figure 16 Calibration curves for each set of calibration data

6 Uncertainty analysis

Thrust measurements by the system have some uncertainty despite all the efforts to minimize the errors. Thus, any reported measurement, should be considered with a precomputed uncertainty. The main sources of measurement uncertainty for an inverted pendulum thrust measurements system are: the calibration procedure, the data acquisition uncertainty, drift of the system between calibrations, and the thrust vector orientation [35]. The sources of uncertainty are analyzed for the studying system for two measurements of 5 mN and 100 mN.
Uncertainty in the calibration procedure can be computed using the calibration equation in form of linear fitting $F = aX + b$. Since the errors in this equation are independent, standard error propagation techniques is used to determine the total uncertainty [27] as followings:

$$\frac{\sigma_F}{F} = \left[\left(\frac{\sigma_a}{a}\right)^2 + \left(\frac{\sigma_X}{X}\right)^2 + \left(\frac{\sigma_b}{b}\right)^2\right]^{1/2} \tag{14}$$

In the above equation, two parameters a and b are found from the calibration data out of the two sensors (LVDT or σ_x and loadcell or σ_f). Therefore, the error for these parameters can be calculated using Eq. (15).

$$\frac{\sigma_a}{a}, \frac{\sigma_b}{b} = \left[\left(\frac{\sigma_f}{f}\right)^2 + \left(\frac{\sigma_x}{x}\right)^2\right]^{1/2} \tag{15}$$

The data acquisition uncertainty is the error of LVDT measurement or σ_x. The third source of uncertainty is drift of the system between calibrations. Experimental tests of the system declare that this error is not more than 2 μm even within the temperature variations. The last uncertainty or the thrust vector orientation depends on the geometry of the system. Using an inclinometer with accuracy of 0.1°, error of the thrust vector orientation becomes $tan(0.1) = 0.0017$. Consequently, total uncertainty of the system for two measurements of 5 mN and 100 mN are calculated as seen in Table (2).
It is clear from the above table that the maximum uncertainty is less than 10% for the minimum thrust measurement and this value decreases as the thrust is increasing. This is due to the fact that some uncertainty values are constant within the measuring range.

7 Conclusion

This paper detailed designing, modeling, manufacturing, calibrating and verifying of a thrust measurement system with inverted pendulum configuration. The system expected to measure thrust forces in a range of 5 to 100 mN, while operating in vacuum condition of 1e-5 mbar and in temperature range within -40°C to +80°C. This was the novelty of the presented system. Designing phase composed of three subsections include structure design, hinge design and thermal design, which were accomplished using optimization techniques and thermal simulations.
All parts of the system were manufactured with high precision from acceptable materials for thermal-vacuum conditions. In order to calibrate and verify the system, an electromagnetic actuator was designed and verified with. Calibration results declared that thermal conditions impacted the thrust measurement system, the actuator and the calibration procedure meaningfully. This is an important matter which must be kept in mind for testing in thermal-vacuum conditions. Finally, overall uncertainty of the system was calculated.

Table 2 Uncertainty analysis

Uncertainty source	5 mN measurement	100 mN measurement
Calibration procedure	1.42%	1.42%
Data acquisition	2.70%	0.13%
Drift	5.41%	0.27%
Thrust vector orientation	0.17%	0.17%
Total uncertainty	9.7%	1.99%

References

[1] K. D. Diamant, J. E. Pollard, M. W. Crofton, M. J. Patterson, and G. C. Soulas, "Thrust Stand Characterization of the NASA Evolutionary Xenon Thruster (NEXT)," in *46th Joint Propulsion Conference and Exhibit*, 2010, Nashville, TN, No. AIAA Paper 2010-6701, doi: 10.2514/1.B34095.

[2] D. Packan, J. Bonnet, and S. Rocca, "Thrust Measurements with the ONERA Micronewton Balance," in *Proceedings of the 30th International Electric Propulsion Conference*, 2007, Florence, Italy, doi: http://electricrocket.org/IEPC/IEPC-2007-118.pdf.

[3] N. Nagao, S. Yokota, K. Komurasaki, and Y. Arakawa, "Development of a Dual Pendulum Thrust Stand for Hall Thrusters," in *43rd AIAA/ASME/SAE/ASEE Joint Propulsion Conference & Exhibit*, 2007, Cincinnati, OH, p. 5298, doi: 10.1063/1.2815336.

[4] A. Grubišić and S. Gabriel, "Development of an Indirect Counterbalanced Pendulum Optical-lever Thrust Balance for Micro-to Millinewton Thrust Measurement," *Measurement Science and Technology*, Vol. 21, No. 10, p. 105101, 2010, doi: 10.1088/0957-0233/21/10/105101.

[5] A. R. Wong, A. Toftul, K. A. Polzin, and J. B. Pearson, "Non-contact Thrust Stand Calibration Method for Repetitively Pulsed Electric Thrusters," *Review of Scientific Instruments*, Vol. 83, No. 2, 2012, doi: 10.1063/1.3680557.

[6] Y. Nakagawa, D. Tomita, H. Koizumi, and K. Komurasaki, "Design and Test of a 100 μN-class Thrust Stand for a Miniature Water Ion Thruster with CubeSat," *Transactions of the Japan Society for Aeronautical and Space Sciences, Aerospace Technology Japan*, Vol. 16, No. 7, pp. 673-678, 2018, doi: 10.2322/tastj.16.673.

[7] H. Xu et al., "A Compound Pendulum for Thrust Measurement of Micro-Newton Thruster," *Review of Scientific Instruments*, Vol. 93, No. 6, 2022, doi: 10.1063/5.0090980.

[8] B. N. Wachs and B. A. Jorns, "Sub-millinewton Thrust Stand and Wireless Power Coupler for Microwave-powered Small Satellite Thrusters," *Review of Scientific Instruments*, Vol. 93, No. 8, 2022, doi: 10.1063/5.0088831.

[9] L. Cassady, A. Kodys, and E. Choueiri, "A Thrust Stand for High-power Steady-state Plasma Thrusters," in *38th AIAA/ASME/SAE/ASEE Joint Propulsion Conference & Exhibit*, 2002, Indianapolis, IN, p. 4118, doi: 10.2514/6.2002-4118.

[10] A. Kodys, R. Murray, L. Cassady, and E. Choueiri, "An Inverted-pendulum Thrust Stand for High-power Electric Thrusters," in *42nd AIAA/ASME/SAE/ASEE Joint Propulsion Conference & Exhibit*, 2006, Sacramento, California, p. 4821, doi: 10.2514/6.2006-4821.

[11] K. G. Xu and M. L. Walker, "High-power, Null-type, Inverted Pendulum Thrust Stand," *Review of Scientific Instruments*, Vol. 80, No. 5, 2009, doi: 10.1063/1.3125626.

[12] A. Neumann, J. Simon, and J. Schmidt, "Thrust Measurement and Thrust Balance Development at DLR's Electric Propulsion Test Facility," *EPJ Techniques and Instrumentation*, Vol. 8, No. 1, p. 17, 2021, doi: 10.1140/epjti/s40485-021-00074-7.

[13] U. Kokal and M. Celik, "Development of a Mili-Newton Level Thrust Stand for Thrust Measurements of Electric Propulsion Systems," in *2017 8th International Conference on Recent Advances in Space Technologies (RAST)*, 2017: IEEE, Istanbul, Turkey, pp. 31-37, doi: 10.1109/RAST.2017.8002970.

[14] H. Harmann, H. Dartsch, and E. Werner, "Low Drift Thrust Balance with High Resolution," in *Joint Conference of 30th International Symposium on Space Technology and Science, 34th International Electric Propulsion Conference and 6th Nano-satellite Symposium*, IEPC-2015-257/ISTS-2015-b-257, 2016, Japan, doi: https://www.ast-space.com/wp-content/uploads/2021/10/IEPC-2015-257-Low_Drift_Thrust_Balance_with_High_Resolution.pdf.

[15] U. Kokal, E. Saridede, and M. Celik, "Development and Tests of a Thrust Stand with an In-situ Null Position Adjustment and Calibration Method for Low Power Plasma Thrusters," *Results in Engineering*, p. 101219, 2023, doi: 10.1016/j.rineng.2023.101219.

[16] J. Asakawa, K. Nishii, Y. Nakagawa, H. Koizumi, and K. Komurasaki, "Direct Measurement of 1-mN-class Thrust and 100-s-class Specific Impulse for a CubeSat Propulsion System," *Review of Scientific Instruments*, Vol. 91, No. 3, 2020, doi: 10.1063/1.5121411.

[17] S. Scharmann, K. Keil, J. Zorn, P. Dietz, B. Nauschütt, K. Holste, K. Hannemann, P. J. Klar, S. Kloss, S. Graubner, A. Neumann, and J. Simon, "Thrust Measurement of an Ion Thruster by a Force Probe Approach and Comparison to a Thrust Balance," *AIP Advances*, Vol. 12, No. 4, 2022, doi: 10.1063/5.0066401.

[18] Y.-X. Yang, L.-C. Tu, S.-Q. Yang, and J. Luo, "A Torsion Balance for Impulse and Thrust Measurements of Micro-Newton Thrusters," *Review of Scientific Instruments*, Vol. 83, No. 1, 2012, doi: 10.1063/1.3675576.

[19] J. Kolbeck, T. E. Porter, and M. Keidar, "High Precision Thrust Balance Development at the George Washington," in *Proceedings of the 35th International Electric Propulsion Conference*, Georgia, USA, 2017, doi: https://www.researchgate.net/publication/320371491_High_Precision_Thrust_Balance_Development_at_the_George_Washington_University.

[20] M. R. Anselmo and R. I. Marques, "Torsional Thrust Balance for Electric Propulsion Application with Electrostatic Calibration Device," *Measurement Science and Technology*, Vol. 30, No. 5, p. 055903, 2019, doi: 10.1088/1361-6501/ab0f0e.

[21] D. L. O. Soares and R. I. Marques, "In Vacuum Dynamic and Static Tests of a Thrust Balance for Electric Propulsion with Hysteresis Analysis and Behaviour Prediction with Transfer Function," *Measurement Science and Technology*, Vol. 32, No. 12, p. 125903, 2021, doi: 10.1088/1361-6501/ac271d.

[22] Y. Zhang, D. Guo, and Y. Yang, "Design and Experimental Validation of a Micro-Newton Torsional Thrust Balance for Ionic Liquid Electrospray Thruster," *Aerospace*, Vol. 9, No. 10, p. 545, 2022, doi: 10.3390/aerospace9100545.

[23] H. Zhang, B. Duan,, L. Wu, Z. Hua, Z. Bao, N. Guo, Y. Ye, L.T. DeLuca, and R. Shen, "Development of a Steady-state Microthrust Measurement Stand for Microspacecrafts," *Measurement*, Vol. 178, p. 109357, 2021, doi: 10.1016/j.measurement.2021.109357.

[24] J. Soni and S. Roy, "Design and Characterization of a Nano-Newton Resolution Thrust Stand," *Review of Scientific Instruments*, Vol. 84, No. 9, 2013, doi: 10.1063/1.4819252.

[25] C. Yang, J.-W. He, L. Duan, Q. Kang, and T. S. Collaboration, "A Torsional Thrust Stand for Measuring the Thrust Response Time of Micro-Newton Thrusters," *International Journal of Modern Physics A*, Vol. 36, No. 11n12, p. 2140015, 2021, doi: 10.1142/S0217751X21400157.

[26] M. R. Gilpin, W. A. McGehee, N. I. Arnold, M. R. Natisin, and Z. A. Holley, "Dual-axis Thrust Stand for the Direct Characterization of Electrospray Performance," *Review of Scientific Instruments*, Vol. 93, No. 6, 2022, doi: 10.1063/5.0087716.

[27] J. E. Polk, J.E. Polk, A. Pancotti, T. Haag, S. King, M. Walker, J. Blakely, and J. Ziemer "Recommended Practice for Thrust Measurement in Electric Propulsion Testing," *Journal of Propulsion and Power*, Vol. 33, No. 3, pp. 539-555, 2017, doi: 10.2514/1.B35564.

[28] J. R. Brauer, *Magnetic Actuators and Sensors*, John Wiley & Sons, 2006, https://catalogue.library.cern/literature/3etgt-j4h30.

[29] G. Shan, Y. Li, L. Zhang, Z. Wang, Y. Zhang, and J. Qian, "Contributed Review: Application of Voice Coil Motors in High-precision Positioning Stages with Large Travel Ranges," *Review of Scientific Instruments*, Vol. 86, No. 10, 2015, doi: 10.1063/1.4932580.

[30] J. Rovers, J. Jansen, and E. A. Lomonova, "Analytical Calculation of the Force between a Rectangular Coil and a Cuboidal Permanent Magnet," *IEEE Transactions on Magnetics*, Vol. 46, No. 6, pp. 1656-1659, 2010, doi: 10.1109/TMAG.2010.2040589.

[31] E. P. Furlani, *Permanent Magnet and Electromechanical Devices: Materials, Analysis, and Applications*, Academic Press, 2001, https://www.google.com/books/edition/_/KjJM8i3tIsQC?hl=en&gbpv=1.

[32] G. Akoun and J.-P. Yonnet, "3D Analytical Calculation of the Forces Exerted between Two Cuboidal Magnets," *IEEE Transactions on Magnetics*, Vol. 20, No. 5, pp. 1962-1964, 1984, doi: 10.1109/TMAG.1984.1063554.

[33] J. Jansen, C. Van Lierop, E. A. Lomonova, and A. Vandenput, "Modeling of Magnetically Levitated Planar Actuators with Moving Magnets," *IEEE Transactions on Magnetics*, Vol. 43, No. 1, pp. 15-25, 2006, doi: 10.1109/TMAG.2006.886051.

[34] J. Compter, E. Lomonova, and J. Makarovic, "Direct 3-D Method for Performance Prediction of a Linear Moving Coil Actuator with Various Topologies," *IEEE Proceedings-Science, Measurement and Technology*, Vol. 150, No. 4, pp. 183-191, 2003, doi: 10.1049/ip-smt:20030586.

[35] J. Mackey, S. J. Hall, T. Haag, P. Y. Peterson, and H. Kamhawi, "Uncertainty in Inverted Pendulum Thrust Measurements," in *2018 Joint Propulsion Conference*, 2018, p. 4516, doi: 10.2514/6.2018-4516.

Nomenclature

English symbols

A, B, C	Dimensions of magnet
B_z	z-component of the magnetic field
C	Damping coefficient
d_c	Diameter of wire
F	Thrust force
g	Earth gravity
H_1	Rotation-arm of the upper mount-plate
H_2	Rotation-arm of the lower mount-plate
h_c	Height of coil
i	Current of coil
J	Inertia moment of system about lower mount-plate CG
J_b	Inertia moment of upper mount-plate about its left end
J_l	Inertia moment of left arm about its CG
J_r	Inertia moment of right arm about its CG
J_u	Inertia moment of lower mount-plate about its left end
K	Torsional stiffness of the strip hinge
L	Length of upper and lower mount-plate
l_c	Length of wire
M	Mass of system
M_s	Magnetization
m_b	Mass of lower mount-plate
m_u	Mass of upper mount-plate
m_l	Mass of left arm-plate

m_r	Mass of right arm-plate
m_t	Mass of thruster
m_c	Mass of counterweights
w_c	Width of coil
θ	Rotation of system
μ_0	Permeability
ω	Fundamental frequency of system